Since January 2020 Elsevier has created a COVID-19 resource centre with free information in English and Mandarin on the novel coronavirus COVID-19. The COVID-19 resource centre is hosted on Elsevier Connect, the company's public news and information website.

Talanta 265 (2023) 124804

Contents lists available at ScienceDirect

Talanta

journal homepage: www.elsevier.com/locate/talanta

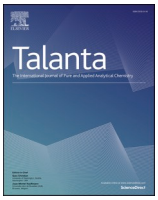

Design of a rapid electrochemical biosensor based on MXene/Pt/C nanocomposite and DNA/RNA hybridization for the detection of COVID-19

Monireh Bolourinezhad [a], Majid Rezayi [a,b], Zahra Meshkat [c], Saman Soleimanpour [d], Majid Mojarrad [e], Farkhonde zibadi [a], Seyed Hamid Aghaee-Bakhtiari [a,f,**], Seyed Mohammad Taghdisi [g,h,*]

[a] Department of Medical Biotechnology and Nanotechnology, Faculty of Medicine, Mashhad University of Medical Sciences, Mashhad, Iran
[b] Medical Toxicology Research Center, Mashhad University of Medical Sciences, Mashhad, Iran
[c] Antimicrobial Resistance Research Center, Department of Medical Bacteriology and Virology, Qaem University Hospital, School of Medicine, Mashhad University of Medical Sciences, Mashhad, Iran
[d] Antimicrobial Resistance Research Center, Bu-Ali Research Institute, Mashhad University of Medical Sciences, Mashhad, Iran
[e] Department of Genetics, School of Medicine Medical Genetics Research Center Basic Sciences Research Institute Mashhad University of Medical Sciences, Iran
[f] Bioinformatics Research Group, Mashhad University of Medical Sciences, Mashhad, Iran
[g] Targeted Drug Delivery Research Center, Pharmaceutical Technology Institute, Mashhad University of Medical Sciences, Mashhad, Iran
[h] Department of Pharmaceutical Biotechnology, School of Pharmacy, Mashhad University of Medical Sciences, Mashhad, Iran

ARTICLE INFO

Handling Editor: Prof. J.-M. Kauffmann

Keywords:
Electrochemical biosensor
SARS-CoV-2
Platinum carbon
MXene nanosheets

ABSTRACT

Since the rapid spread of the SARS-CoV-2 (2019), the need for early diagnostic techniques to control this pandemic has been highlighted. Diagnostic methods based on virus replication, such as RT-PCR, are exceedingly time-consuming and expensive. As a result, a rapid and accurate electrochemical test which is both available and cost-effective was designed in this study. MXene nanosheets (Ti_3C_2Tx) and carbon platinum (Pt/C) were employed to amplify the signal of this biosensor upon hybridization reaction of the DNA probe and the virus's specific oligonucleotide target in the RdRp gene region. By the differential pulse voltammetry (DPV) technique, the calibration curve was obtained for the target with varying concentrations ranging from 1 aM to 100 nM. Due to the increase in the concentration of the oligonucleotide target, the signal of DPV increased with a positive slope and a correlation coefficient of 0.9977. Therefore, at least a limit of detection (LOD) was obtained 0.4 aM. Furthermore, the specificity and sensitivity of the sensors were evaluated with 192 clinical samples with positive and negative RT-PCR tests, which revealed 100% accuracy and sensitivity, 97.87% specificity and limit of quantification (LOQ) of 60 copies/mL. Besides, various matrices such as saliva, nasopharyngeal swabs, and serum were assessed for detecting SARS-CoV-2 infection by the developed biosensor, indicating that this biosensor has the potential to be used for rapid Covid-19 test detection.

Authors' contributions

All authors have read and approved the final manuscript.

Lead author: Name: *Monireh Bolourinezhad.*

Disclosure: *Investigation, Conceptualization, Methodology, Formal analysis, Writing - original draft. She has no conflict of interest about this article.*

Corresponding author: Name: Seyed Mohammad Taghdisi.

Disclosure: Supervision, Conceptualization, Investigation, Methodology, Formal analysis, *Writing - review & editing. He has no conflict of interest about this article.*

Corresponding author: Name*: Seyed Hamid Aghaee-Bakhtiari.*

Disclosure: *Project administration, Investigation, Methodology, Formal analysis, Writing - review & editing. he has no conflict of interest about this article.*

Coauthor: Name*: Majid Rezayi.*

Disclosure: *Investigation, Conceptualization, Methodology, Writing - review & editing,* Funding *acquisition, he has no conflict of interest about this article.*

Coauthor: Name: *Zahra Meshkat.*

* Corresponding author. Targeted Drug Delivery Research Center, Pharmaceutical Technology Institute, Mashhad University of Medical Sciences, Mashhad, Iran.
** Corresponding author. Medical Biotechnology and Nanotechnology, Mashhad University of Medical Sciences, Mashhad, Iran.
E-mail addresses: AghaeiBH@mums.ac.ir (S.H. Aghaee-Bakhtiari), taghdisihm@mums.ac.ir (S.M. Taghdisi).

https://doi.org/10.1016/j.talanta.2023.124804
Received 10 March 2023; Received in revised form 29 May 2023; Accepted 9 June 2023
Available online 12 June 2023

Disclosure: *Methodology, Formal analysis, Resources, Writing - review & editing, she has no conflict of interest about this article.*

Coauthor: Name: *Saman Soleimanpour*.

Disclosure: *Methodology, Formal analysis, Resources, Writing - review & editing, he has no conflict of interest about this article.*

Coauthor: Name: *Majid Mojarrad*.

Disclosure: *Methodology, Formal analysis, Writing - review & editing, he has no conflict of interest about this article.*

Coauthor: Name: *Farkhonde zibadi*.

Disclosure: *Writing - review & editing, Formal analysis, she has no conflict of interest about this article.*

1. Introduction

Coronaviruses are RNA viruses classified into four different genera (alpha, beta, gamma, and delta). Six types of these viruses have been previously found to cause mild respiratory diseases (alpha types: 229E and NL63-beta types: OC43 and HKU1) and severe respiratory diseases (beta types: SARS and MERS) in humans [1]. In December 2019, a new strain of this family was identified in Wuhan, China [2], with a 3 kb long single-stranded positive RNA genome. Because of its high rate of transmission, developing a procedure for diagnosing this disease is essential [2]. The World Health Organization has confirmed RT-PCR as one of the most frequent molecular diagnostic tests for SARS-CoV-2 [3,4]. However, this test has its own limitations, including the need for specialized laboratory personnel, laboratory equipment, and a relatively high cost. Additionally, even though these standard tests are sensitive, false negatives and positives are seen during sampling errors and sample types [5,6]. Rapid serological tests are also based on Ag/Ab binding; while they are highly sensitive, they cannot be employed in the early stages of the disease when the immune system is not still active [7,8]. Therefore, substantial research was required to develop fast diagnostic tests that could be utilized at home or in small clinics [9].

In the recent years, the use of electrochemical biosensors, that can detect and represent biomolecular targets based on electrochemical reactions, has received much attention for the detection of infectious agents [10–17]. The construction of an electrochemical biosensor, which is frequently based on several nanoscale approaches such as signal amplification method [18–20], is necessary for the practical use of electrochemical technology for the detection of a nucleic acid fragment [21–23]. Among them, two-dimensional nanomaterials, including graphene, boron nitride, graphite carbon nitride, MXenes, and black phosphorus, have received considerable attention in electrochemical biosensors to build a suitable electrical conductive matrix with more efficient surfaces due to the small size of nanoparticles [20,24–29]. Given its excellent flexibility and strong electrical conductivity, MXene has outperformed all other 2D nanomaterials which have been utilized to develop electrochemical-sensors [30,31]. Additionally, diverse organic linkers, including thiol, silica, conductive polymers, etc., are frequently used on the surface of 2D nanomaterials for DNA electrochemical biosensors to create hybrids with a DNA structure. Due to the fact that MXene can be attached to DNA without the need for a specific linker, many easy-to-construct electrochemical biosensors have been developed [32–34]. Besides, to have especially synergetic effects of nanomaterials such as strong electrochemical signal and more surface area, MXene Ti_3C_2Tx combined with other nanomaterials have been designed for DNA electrochemical sensors [35]. For example MXene-Au and MoS_2/Ti_3C_2 nanocomposites had been developed to detect microRNA-377 [36] and miRNA-21 [36] respectively.

To accurately detect COVID-19, this study introduced a rapid electrochemical biosensor based on DNA/RNA hybridization and MXene combined with Pt/C as an excellent signal amplifier. SARS-CoV-2 genomes from the GISATD and NCBI were then analyzed to design a conserved sequence of oligonucleotide probes to identify the potential genomic regions in RNA samples. MXene/Pt/C nanocomposite was then prepared and applied to modify the surface of the sensor. The calibration curve was obtained for the target with different concentrations range of 1 aM–100 nM, which was labeled with methylene blue (MB) as a redox indicator, by differential pulse voltammetry (DPV) technique with at least a limit of detection (LOD) and quantification (LOQ) 0.4 aM and 60 copies/mL. Additionally, the specificity and sensitivity of this sensor for the detection of COVID-19, compared to other respiratory viruses was assessed by the RT-PCR method for 192 clinical sample patients, which revealed 100% accuracy, sensitivity, and 97.87% specificity. The potential ability of the biosensor in different matrices of serum, saliva, and nasopharynx was obtained. The resulting biosensor could be possible for a clinical application requiring a specific, sensitive, and quick diagnosis of COVID-19.

2. Experimental section

2.1. Chemicals and, instruments

Detailed information about the reagents and equipment can be seen in the supplementary file.

2.2. Synthesis of MXene

All experimental data related to the synthesis of MXene can be found in the additional data file.

2.3. Designing a specific sequence of a probe

One of the essential things to increase the specificity and sensitivity of the DNA sensors is to design a specific and accurate probe sequence. The probe was intended for the SARS-CoV-2 virus genome, as well as other oligonucleotides (complementary and non-complementary) in silico; based on the sequence of RNA-dependent RNA polymerase gene (RdRP) inside the ORF1ab open reading frame region, which has been published as a conserved region [37]. Approximately 22 sequences encoding RdRP from different geographical areas were taken from NCBI, GenBank, as listed in Table S1. Then, sequences were clustered by ClustalW algorithm of Bio Edit sequence alignment editor v 7.2.5 [38] to from the highly conserved areas of the Orf1ab gene. A number of possible probe sequences were then chosen using Gene runner software, version 6.0.11, with the optimum energy of binding and disruption, and 1 M sodium chlorides; also, temperature of folding was close to the ambient temperature of 37 °C and the suitable length consisted of 21 nucleotides (Table S2) [39]. Finally, the probe specificity was confirmed again by the BLASTn nucleotide (https://blast.ncbi.nlm.nih.gov/Blast.cgi). So, the selected probe could only be used specifically for SARS-CoV-2 virus detection and comprised information on the genetic sequence. Hot spots of the clinical and epidemiological data relevant to the geographic features of this specific sequence were analyzed by the GISAID database [40].

2.4. Sensing platform fabrication

To modify the electrode, the surface of the electrode can be made clean by polishing it with aluminum hydroxide powder. After 1 min in a solution of water and ethanol (1:1), the electrode was then dropped with 6 μL of this nanocomposite (1 mg of Ti_3C_2 dispersed in ultra-pure water and mixed with 1 mg Pt/C solved with 200 μL of isopropanol and 2 μL of 5 wt% Nafion solution under 20 min ultrasonication to form the complete composite), which had to be dried at room temperature. After that, 6 μL of the 500 nM probe in 0.05 M HEPES buffer solution, 1 mM Mn^{2+} (pH 7.5) was used to drop and stabilize the probe on the surface of the electrode for 1 h at room temperature; then the electrode three times were washed with 0.05 M phosphate buffer saline (PBS) to eliminate the destabilized DNA probe. Finally, 3 μL of 0.1% of bovine serum albumin (BSA) was added to the electrode surface and left at room temperature to improve the test specificity and minimize empty spaces left by the probe

sequence and rinsing was done for 1 min in the PBS (pH 7, 0.05 M).

2.5. Electrochemical measurement

All electrochemical measurements were performed by the Atolab device three times at room temperature using the differential pulse voltammetry technique (DPV) in PBS (pH 7, 0.05 M), in the potential range of −0.6 to +0.6 V, with the sample width of 0.0167 s, pulse width of 0.05 s and pulse amplitude of 0.05 V. The organic dye, methylene blue (MB), was then utilized to label target as a redox marker in the DPV technique to identify the hybridization event. Upon integration with the DNA framework, MB undergoes two-electron reduction and is rapidly converted into leucomethylene blue, thereby generating an electric signal. Within the scope of this research, MB was employed to identify and mark the complementary DNA strands relevant to our target. This can be attributed to either MB's affinity for guanine bases present on DNA molecules or its electrostatic interaction with anionic DNA due to cationic properties. Subsequently, the electrochemical conduct of ssDNA or SARS-CoV-2 RNA in complementary proportions was analyzed by tagging them with 5 μL PBS containing 500 nM Mb [41–43]. The electrochemical behavior of complementary ssDNA or SARS-CoV-2 RNA tagged with MB was assessed after 30 min incubation time with a modified electrode. Then, the modified electrode was washed with PBS to eliminate unfixed sequences, and DPV measurements were conducted. the peak current of the MB largely increased which illustrated more dsDNA-MB accumulation on the electrode surface due to the more electrostatic interactions and intercalation of MB in the DNA double helix.

For electrochemical characterization, CV and electrochemical impedance spectroscopy (EIS) measurements were done in 1 mM $[Fe(CN)_6]^{-3/-4}$ containing 0.1 M KCl. The CV voltammograms were then recorded between - 0.6 V and +0.6 V with scan rates of 10–200 mV/s. EIS measurements were recorded at a frequency range of 10–100 kHz with an amplitude of 10 mV. The construction process and sensing mechanism of the biosensors are presented in Scheme 1.

2.6. Clinical samplespreparation

RNAs of 192 clinical samples with positive results from RT-PCR tests were extracted using the QIAamp Viral RNA Qiagen kit, from

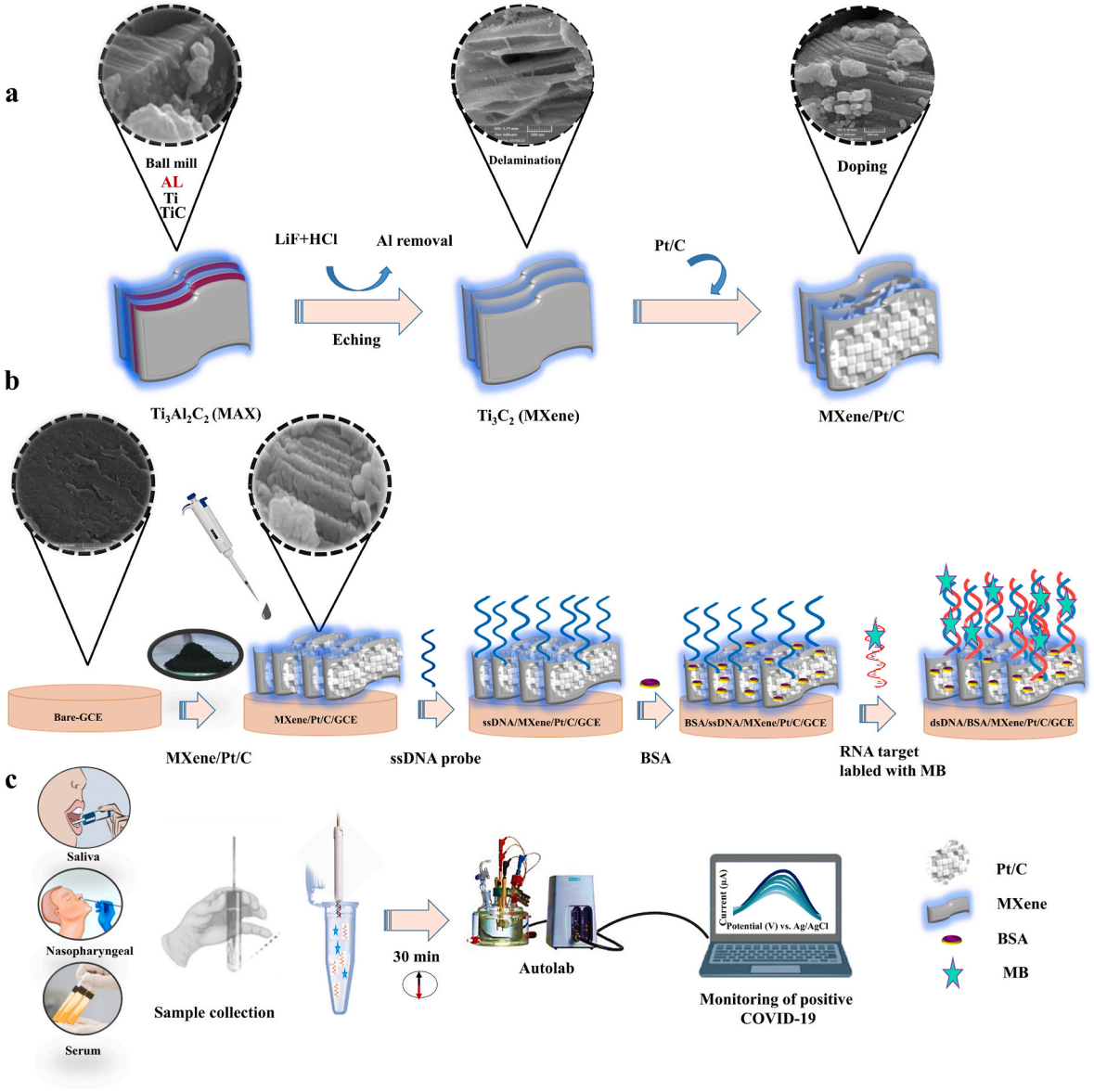

Scheme 1. (a) Synthesis of MXene and MXene/Pt/C. (b) Fabrication the DNA/nano/biosensor. (c) Electrochemical detection process using Autolab device.

nasopharyngeal samples provided by Imam Reza Hospital (Mashhad, Iran) from unnamed COVID-19 patients. The prepared samples were kept in a freezer at −80 °C before use. A commercial one-step Taqman PCR Time Real PCR, Pishtaz Teb Diagnostic COVID-19 RT-PCR Kit was then used in the RT-PCR tests (Pishtaz Teb, Iran). The nasopharyngeal, saliva, and serum samples of healthy people were obtained from Imam Reza Hospital and stored in RNase-free microtubes at 4 °C until use. The positive nasopharyngeal samples were then inactivated by heating them at 56 °C for 30 min, and all real samples were diluted 20 times with PBS (pH 7, 0.05 M).

3. Results and discussion

3.1. Characterizations of the nanocomposite

Fig. 1 illustrates the morphological examination of the MXene/Pt/C

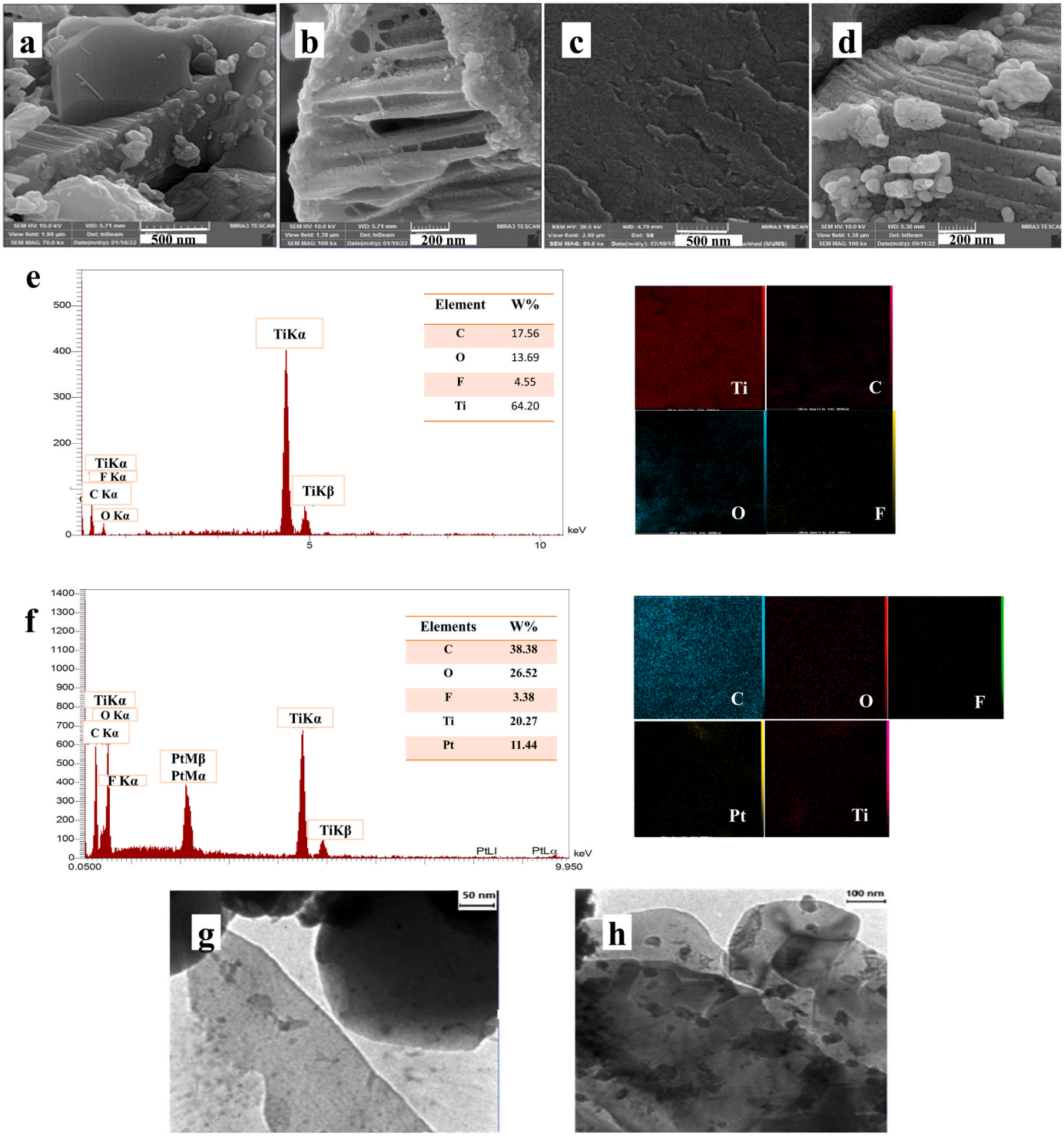

Fig. 1. (a) SEM image of MAX. (b) SEM image of MXene nanosheets. (c) SEM image of bare/GCE (d) SEM image of MXene/Pt/C/GCE. (e) EDX analysis and corresponding elemental mapping data of MXene nanosheets. (f) EDX analysis and corresponding elemental mapping data of MXene/Pt/C. (g) TEM image of MXene nanosheets. (h) TEM image of MXene nanosheets/Pt/C.

nanocomposite using SEM images of the MAX precursor and intercalated MXene along with Energy Dispersive X-ray spectroscopy (EDS) and an EDS elemental map [44]. In the SEM picture of MAX and MXene nanoparticles, following the etching procedure, the formation of the multilayer was visible (Fig. 1a and b). Following the etching procedure, the formation of the multilayer is visible. Since TiO_2 nanoparticles occur on MXene surfaces as a result of the rapid oxidation of titanium carbide under aqueous and oxygen conditions, they appeared like crystal particles on the borders of MXene layers [45]. SEM images of the bare/GCE and Ti_3C_2/Pt/C nanocomposite were used to determine the electrode modification coatings (Fig. 1c and d). By applying an EDS along with an EDS elemental map, the sample composition was ascertained (Fig. 1 e, f and Fig. S1), and the etching operation eliminated the Al element from the precursor, predicting that C, O, F, Pt, and Ti elements were distributed and coexisted uniformly across the entire scanning area. MXene nanosheet synthesized and Pt/C growth on the surface of Ti_3C_2 could be seen through transition electron microscopy (TEM) images (Fig. 1g and h) which revealed individual layer and multilayer of MXene/Pt/C flakes of micron size [46]. Fourier Transformed Infrared (FTIR) and prior data spectrum (XRD) analysis were also used to evaluate the chemical properties of the synthesized MXene nanosheets. The FTIR spectrum of Ti_3AlC_2 included bands of TiO_2, TiO, AlO, CH, and CH_2 at 482, 597, 1005, 1537, and 2831 cm^{-1} peaks (Fig. S2a). Additionally, the FTIR spectrum was used to analyze the functional groups on the surface of Ti_3C_2. The stretching vibrations of –OH, C═O, O–H, C–F, and Ti–O bonds were responsible for the 3430 cm^{-1}, 1630 cm^{-1}, 1390 cm^{-1}, 1100 cm^{-1}, and 662 cm^{-1} peaks (Fig. S2b), which were in agreement with the prior data [47]. For the XRD analysis, the (002), (004), (101), (103), (104), (105), (107), (108), and (109) planes of the Ti_3AlC_2 MAX phase were correlated to a sequence of distinctive peaks at $2\theta = 9.43°$, 18.90°, 34.12°, 36.22°, 38.8°, 41.81°, and 48.43°, as illustrated in Fig. S2. According to Wang and Zhou's, all peaks were labeled following the Ti_3AlC_2 standard spectrum [45]. According to XRD, Al etching results could be distinguished by XRD measurement at $2\theta = 38.8°$, and "Al"(104) peak of Ti_3AlC_2 was removed from the MAX phase. Further information is provided in the supplementary section.

At $2\theta = 38.8°$, the "Al"(104) peak of Ti_3AlC_2 is notably high. To achieve a higher layer spacing in MXene, it is imperative to completely eliminate the "Al" component from Ti_3AlC_2.The resulting peaks get larger, weaker, and rougher as a result of the etching process. This shows the degree of plane disorderliness, the disappearance of the Ti_3AlC_2 crystal structure, and the formation of a new network of layered material. Another fascinating change was the (002) peak in the spectra of MXene sliding rearward. This was accomplished by etching the AL out of the Ti_3AlC_2 crystal and substituting it with F and/or OH. An increase in the c-lattice parameter might be able to explain this shift (35). The multilayer Ti_3C_2Tx samples are electrically conductive during the MAX phase etching, therefore this increase is then attributed to the layered

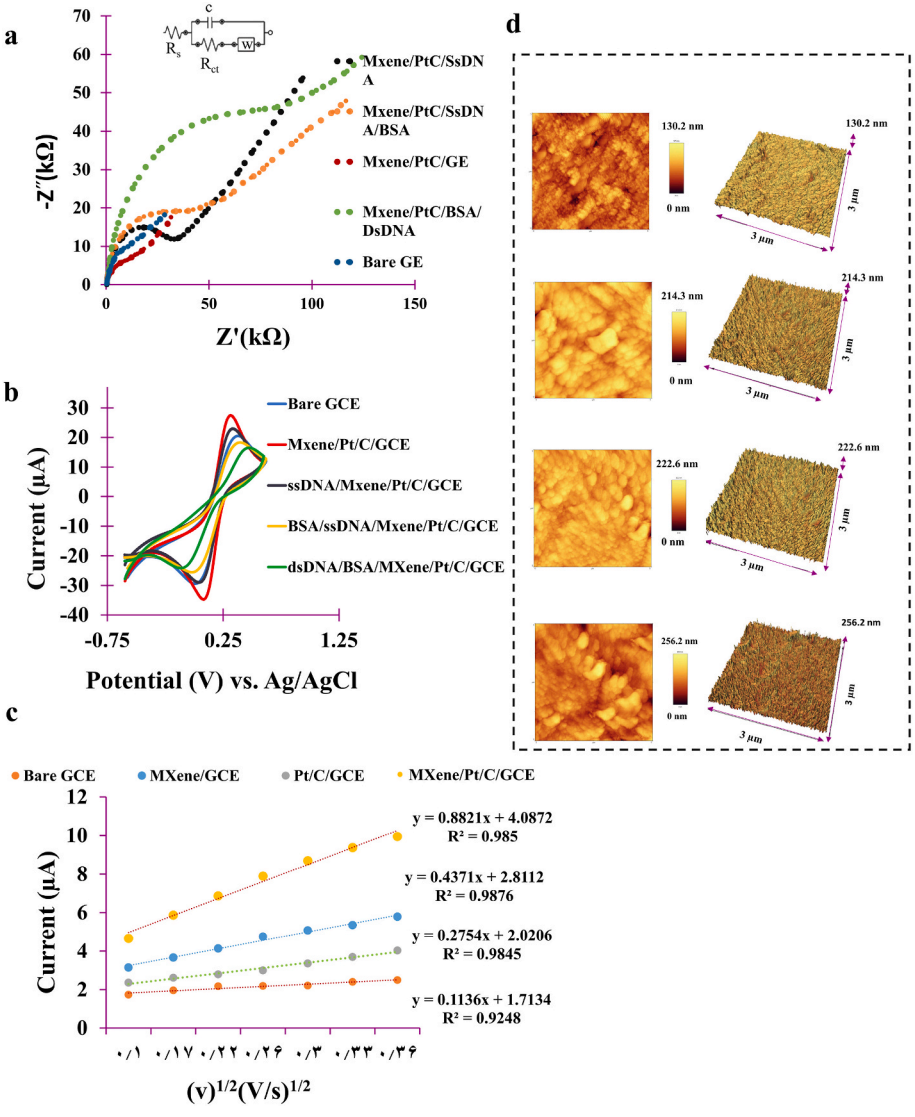

Fig. 2. (a) EIS of various modified electrodes in 5 mM $[Fe(CN)_6]^{-3/-4}$ containing 0.1 M KCl: bare GCE, MXene/Pt/C/GCE, ssDNA/MXene/Pt/C/GCE, and dsDNA/MXene/Pt/C/GCE. (b) CV of various modified electrodes in 5 mM $[Fe(CN)_6]^{-3/-4}$ containing 0.1 M KCl: bare GCE, MXene/Pt/C/GCE, ssDNA/MXene/Pt/C/GCE, and dsDNA/MXene/Pt/C/GCE. (c) Linear curves of bare GCE, MXene/GCE, Pt/C/GCE, MXene/Pt/C/GCE in 5 mM $[Fe(CN)_6]^{-3/-4}$ containing 0.1 M KCl at different scan rates (10–200 mV/s). (d) AFM images of MXene/Pt/C/GCE, ssDNA/MXene/Pt/C/GCE, and dsDNA/MXene/Pt/C/GCE.

structure of MXene.

3.1.1. Characterization of the surface electrode

3.1.1.1. Electrochemical method. Fig. 2 depicts the results of an investigation into various activities of modification steps involved in the developed biosensors using EIS and CV, as well as the redox marker $[Fe(CN)_6]^{-3/-4}$ They were used to bettering understand how the electrode surface's impedance changed when the surface of electrodes were modified.

For EIS, the semicircle at 0.19 V over the frequency range of 1 Hz–100 kHz represented the electron transfer resistance (Rct) to which the electrode interfaces were associated (Chen et al., 2019b). The small semicircle domain on the MXene/Pt/C/GCE electrode revealed that $[Fe(CN)_6]^{-3/-4}$ had more potential to move electrons rapidly than the bare GCE electrode, thus indicating the impact of nanoscale on the electroactive surface area. In addition to the considerable steric-hindrance impact of the negatively charged backbone of DNA strands, it was responsible for the increase of Rct during the strands of DNA immobilization and hybridization (Fig. 2a) [48]. The above results, thus, demonstrated that the biosensor interface had been built efficiently as they could be compared favorably to the results obtained from CV; on the bare GCE, two different redox peaks could be recognized (Fig. 2b). The redox peak currents increased, as compared to the bare surface of electrodes after they were doped with MXene/Pt/C/GCE, thus, demonstrated that the large sheet-like layers of conductivity nanocomposites improved the electrode active surface area while also enabling electron transfer there. Also, in the EIS analysis after treatment with BSA, DNA probe, and target, the peak current of $[Fe(CN)_6]^{-3/-4}$ was significantly reduced [49,50]. The augmented obstacle to electron transfer on modified electrodes is attributed to the negative surface charge. The phosphate chain of probe, with its negatively charged constituents, serves as a convenient explanation for the impeded migration of electrons towards the electrode's surface. Then, after treatment with probe A, the peak current of $[Fe(CN)_6]^{-3/-4}$ is greatly reduced. After the BSA electrode blockage, a decrease in peak current was observed. This reduction became more pronounced with the presence of dsDNA structures, indicating that DNA hybridization resulting from target DNA injection may enhance this effect. The conducted CV and EIS experiments effectively demonstrated the successful creation of a biosensing platform.

Furthermore, the charge cyclic voltammograms of 3 electrodes (bare GCE, MXene/Pt/C/GCE, and Pt/C/GCE) were taken at different scan rates (10–450 mV/s) to further explain how the nature of nanoscale MXene/Pt/C/GCE affected the contact area and resulted in the observed redox peaks. This is illustrated in Fig. 2c. Peak current increases coincided with a rise in scan rates, thus demonstrating that the peak was raised currents rise linearly ($R^2 = 0.9248–0.9876$) in proportion to the square roots of the scan rates. The effective surfaces of bare, MXene/GCE, Pt/C/GCE, and MXene/Pt/C/GCE were analyzed using Randles-Sevich, which were 0.2 Cm^{-2}, 0.38 Cm^{-2}, and 0.77 Cm^{-2}, respectively [51]. After using the nanocomposite to modify the surfaces, there was a four-fold increase in the surfaces. These findings have significantly enhanced the efficacy of nanocomposites in augmenting the electrode surface area for developing DNA probes, which can be utilized to detect hybridization events in future applications.

3.1.1.2. Atomic force microscopy method (AFM). MXene/Pt/C-GCE, MXene/Pt/C-ssDNA probe, and MXene/PTC-dsDNA following hybridization, were all studied by utilizing AFM. AFM images of the MXene/Pt/C/electrode, especially in comparison to the bare electrode, revealed that the surface was entirely covered by a flat multilayer coating of the synthesized MXene/Pt/C nanocomposite and mean width of profile elements (RSM) was increased from 133.73 to 170.48 nm. The increase in the RMS roughness up to 214.3 nm of ssDNA/MXene/Pt/C/GCE, as compared to the MXene/Pt/C/GCE signal, illustrated the accumulation of the ssDNA probe on the electrode surface via the electrostatic interaction between the phosphate backbone of DNA and the altered positive potential by Mn^{2+} that happened when DNA molecules were adsorbed (Fig. 2d). After the hybridization process, the RMS roughness went up even more (222.25 nm), which proved that the hybridization process had occurred on the surface of the biosensor [52].

3.2. Optimization assays

To create a biosensor with high specificity and sensitivity, the operational parameters, including the experimental conditions of the probe and buffer in the biosensor manufacturing stage, were examined and optimized. Also, in the biosensor sensing stage, two essential parameters, including hybridization temperature, and duration, were examined to have the best conditions for electrochemical biosensing based on the DNA/RNA hybridization technique. In both stages of making the biosensor and sensing the target, the current of DPV signal change was used to analyze how well the experimental conditions could be optimized, as explained in the supplementary section (Fig. S3).

3.3. Evaluation of the analytical performance of the COVID-19 biosensor

3.3.1. Sensitivity investigation

DPV measurements were carried out under ideal experimental conditions using different amounts of synthetic target DNA and RNA extracted from real samples (preparation details are explained in the supplementary section (Fig. S4) diluted in a concentration range of 1 aM–100 nM and 1:10 to $1:10^7$ copies/mL in the PBS buffer (pH 7, 0.05 M) which tagged with 5 μL of PBS containing 500 nM Mb to test the sensitivity performance of the proposed biosensor. The electrochemical response indicated a significant increase in peak current of MB which can be attributed to greater accumulation of dsDNA-MB on electrode surface owing to increased intercalation and electrostatic interactions between DNA double helix and MB. As the concentration of target sequences was increased, the output current oxidation of MB was sporadically raised, as depicted in Fig. 3a, c. A satisfactory linear relationship between the current of DPV signal and the logarithm of target concentration was discovered too, as shown in Fig. 3b, d. The corresponding linear equation of I (A) = 0.1015 logC + 2.09 with R2 = 0.9977, and a limit of detection of 0.4 aM for the synthetic target, and I (A) = 0.169logC + 2.4 with R2 = 0.9943 beside the lowest quantified amount of 60 copies/mL for the viral load of a real sample, were determined according to data analysis LOD = 3.3(Sy/S) and LOQ = 10 (Sy/S).

In the realm of electrochemical biosensors, a pioneering effort has been made to ascertain the efficacy of limit detection and quantification by analyzing both synthetic as well as real targets (RNA extracted from genuine samples) for sensitivity and specificity. As evidenced by the data presented in Table 1, our developed biosensor exhibited a remarkably extensive linear range and an ultrasensitive limit of detection for attomolar concentrations and minimum copies/mL when compared to previously established electrochemical techniques. The proposed biosensor exhibits significant potential for clinical application, owing to its remarkable capacity to operate efficiently with intricate matrices like nasopharyngeal swabs, serum and saliva samples. Moreover, it has demonstrated commendable stability when tested on clinical patient specimens. The Antibody/Antigen-based electrochemical sensors [12, 53] and nucleic acid-based electrochemical sensors for detecting

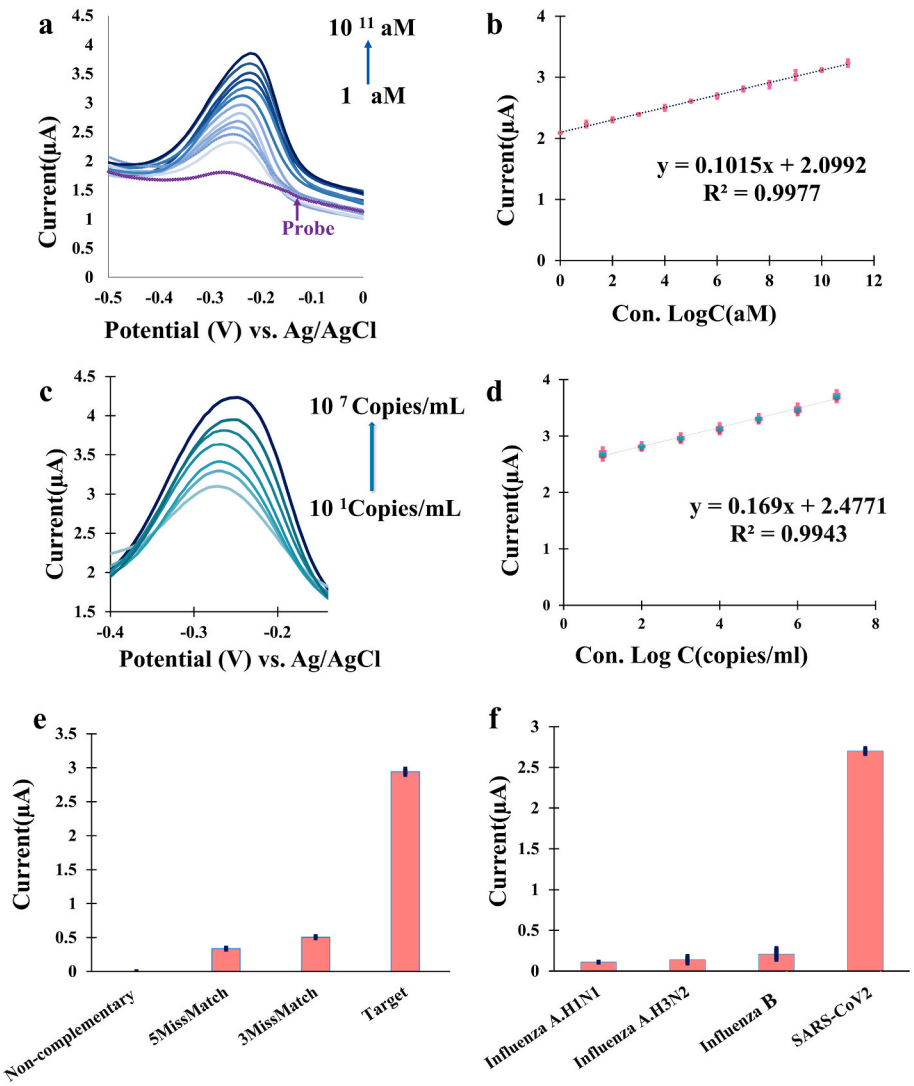

Fig. 3. (a) Sensitivity investigation in the range of 10–10^{11} aM of the synthetic target. (b) The resulting calibration plots for log mol/l. (c) Sensitivity analysis in the range of 10-10^{7} copies/mL of extracted RNA from clinical samples. (d) The resulting calibration plots for log copies/mL. (e) Investigation of specificity using synthetic targets with 5 and 3 mismatch and non-complementary sequences. (f) Specificity investigation using different subtypes of influenza A, H1N1 and H3N2 RNAs, and influenza B RNA from positive real samples. The error bars represent the standard deviations measured by three independent measurements.

Table 1
The comparison our method with the previous electrochemical methods for SARS-CoV-2 detection.

Types of biosensor	Technic	Target analytic	Nano sensor	Limit of detection (LOD)	Linear range	Reference
Antibody/Antigen-based electrochemical sensors	(SWV)	IgG and IgM protein	GO nanosheet	0.11 ng/mL	1–1000 ng/mL	[12]
	(DPV)	Spike and Nucleocapsid protein	Carbon black	19 ng/mL and 8 ng/mL	0.01–0.6 μg/mL	[53]
	(SWV)	Spike protein	–	0.96 and 0.14 ng/mL	1–1000 ng/mL	[12]
Nucleic acid based electrochemical sensors	(DPV)	ORF1ab	Gold nanomaterial MB-CDs	2.2 aM	10.0 aM to 10.0 nM	[43]
	(DPV)	N	AuNPs	231 copies/μL	585.4 copies/μL to 5.854 × 107 copies/μL	[56]
	(DPV)	ORF1ab	Au@Fe3O4	200 copies/mL	10^{-17}-10^{-12} M	[56]
	(DPV)	RdRp	Graphene oxide nanocolloids	186 × 10^{-9}M	10^{-10} to 10^{-5}M	[55]
	(DPV)	N	Electropolymerized polyaniline (PANI) nanowires	3.5 fM	10^{-14} to 10^{-9} M	[54]
	(DPV)	ORF1ab	MXene/Pt/C nanocomposite	0.4 aM	1 aM to 100 nM	Our work

particular SARS-CoV-2 genomes (N gene, S gene, and RdRp gene) [43,54,55] also demonstrate great performance with appropriate LOD. Several electrochemical biosensors are currently being developed which have a quantitation limit of 200 copies/mL [56]. However, these methods still require laborious preparation procedures, skilled personnel, advanced equipment and prolonged analytical periods. Consequently, our novel MXene-based electrochemical biosensor provides advantages such as ease-of-use, rapid analysis timeframes and affordability for on-site monitoring through the use of portable potentiostats that can be operated by anyone.

3.3.2. Selectivity investigation

To test the biosensor selectivity, we utilized synthetic targets with a three-base mismatch, five-base mismatch, and a non-complementary sequence with unique concentrations of 1 pM. This showed that the hybridization of the probe with mismatch components significantly reduced the flowing current of the DPV signal. Additionally, the current for the non-complementary nucleic acid segment was negligible (Fig. 3e). RNA isolated from influenza patients was utilized to assess sensitivity in real samples by employing two different subtypes of influenza A, H1N1, and H3N2 RNAs, as well as influenza B RNA as a target. As a result, the DPV response of the biosensor was not very noteworthy. As can be seen in Fig. 3f, these results showed that we were unable to identify cross-reactivity between influenza A/B viruses and COVID-19.

3.3.3. Evaluation of the accuracy of the biosensor for clinical trials

The findings related to 192 RNA samples were recorded in the box-diagram. The cutoff values were determined to be 0.78 using the IUPAC technique; this means the current of the DPV signal intensities greater than 0.78 were classified as COVID-19 positive [57]. Receiver operating characteristic (ROC) curves were also drawn to assess the methods' capacity for discrimination (Fig. 4a). The suggested biosensor had improvement with 97.87% specificity and 100% sensitivity for differentiating COVID-19 negative samples from positive ones, as evidenced by the biosensor's results for the area below the curve (AUC), which was 0.9. A T-test was also run to determine the importance of the variance between the positive and negative groups. Considerable differences between the two groups of samples were discovered, with the results ($p = 0.0001$, Fig. 4b). Furthermore, to improve the higher sensitivity of biosensor rather than RT-PCR, successive dilutions of the isolated RNA samples (dilution ratios from 1:10 to $1:10^{12}$) were carried out using SARS-CoV-2 RNA extracted from positive patient samples with a cycle threshold (Ct) of 20. These samples were analyzed by the proposed biosensor and RT-PCR to re-determine the Ct of the diluted samples for the purpose of comparison. SARS-CoV-2 RNA was detected even after a 10^8-fold to10^{12} dilution by the biosensor, but the RT-PCR approach provided positive samples only at a 10^8-fold dilution of SARS-CoV-2 RNA (Fig. 4c). The sensitivity of our biosensor was 100 times more than that of RT-PCR. This showed that the LOD of the Pishtaz Teb Medical diagnostic COVID-19 RT-PCR Kit used in this experiment, was 200 copies/mL on Ct = 32. Our biosensor had previously done the measurement at the LOQ of 60 copies/mL.

3.3.4. Analysis of the performance of the biosensor using various matrices

To better analyze the performance of the biosensor, the sensitivity of the biosensor was examined in different sampling matrices. The non-invasive gold standard for coronavirus illness is a nasopharyngeal swab, but its accessibility is limited by the requirement for specialized laboratory knowledge sampling. Serums, as invasive samples, should be theoretically the ideal input for a viral test since they contain a variety of signs the body excretes, such as cell-free DNA and cell-free RNA. Saliva is a preferred alternative because of the virus's high load of 1–2 10^8 infectious copies/mL. The extracted RNA target was spiked in nasopharyngeal swabs, healthy people's serum, and saliva samples that included RNase inhibitors at target concentrations between 1 and 10^7 copies/mL. As a result, calculations for nasopharyngeal swabs, serum, and saliva samples were done (Table 2). These calculations showed not only the good efficiency recovery (90.4–111.6%) and good repeatability (RSD% from 2.8% to 4.8%) of different concentrations in various matrices, but also confirmed the lowest quantified amount, which was calculated to be 60, 50, and 70 copies/mL for nasopharyngeal swabs, serum, and saliva samples, respectively. This demonstrated the

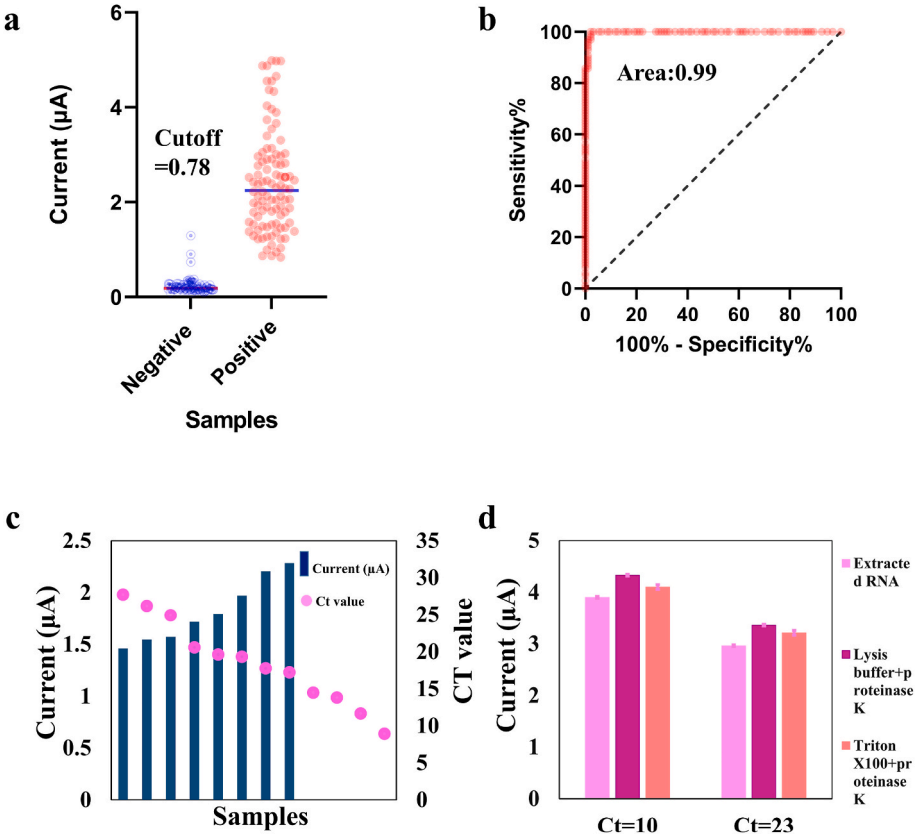

Fig. 4. (a) ROC analysis to assess the detection capability of the biosensor. (b) comparison of the DPV signal to the Ct value of real-time PCR (c) Box-diagram for the quantitative detection of SARS-CoV-2 RNA in 192 clinical samples. (d) Evaluation of a biosensor's performance in clinical RNA extracted samples, real samples with lysis buffer and proteinase K, and real samples with Triton X100 and proteinase K.

Table 2
Comparison of the performance of this biosensor using various matrices: PBS, saliva, serum, and nasopharyngeal.

Matrices	Regression equation	LOQ (Copies/mL)	Linear range copies/mL	Recovery (%)	Relative standard deviation (%)
PBS	$y = 0.169x + 2.4771$ $R^2 = 0.9943$	60	$10–10^7$	95–105	2.2–4.0
Saliva	$y = 0.1528x + 2.327$ $R^2 = 0.9408$	60	$10–10^7$	90.4–105	2.8–4.3
Serum	$y = 0.0966x + 1.7956$ $R^2 = 0.9881$	50	$10–10^7$	95–107	3.2–4.8
Nasopharyngeal	$y = 0.1895x + 3.2737$ $R^2 = 0.9732$	70	$10–10^7$	97–111.6	2.9–4.0

effectiveness of this biosensor in a variety of matrices, even in a serum sample with a minimal viral load of 80.4–187.5 copies/mL.

3.3.5. Evaluation of the biosensor performance in the clinical samples without the extraction step

The nasopharyngeal samples of the patients with high and low virus levels (low and high Ct = 10 and 23) were placed at 60 °C for 30 min and 90 °C for 5 min to ensure safety and evaluate the effectiveness of the developed biosensor as a rapid diagnostic test. It should be noted that proteinase K was used at a rate of 1.25 mg/mL of the sample to prevent RNA degradation caused by nucleases; also, TritonX-100 0.5% was applied for one sample to induce cell lysis, as well as the release of virus from the cytoplasm. The lysis buffer from the Novin gene RT-PCR kit was utilized for the second sample at 1000 μL/mL. Fig. 4d compares the current of the DPV signal acquired from the biosensor after introducing real samples without RNA extraction. As can be seen, compared to use of extracted RNA, a very tiny increase in the output signal was observed for non-extracted methods, which was correlated to the presence of macromolecules in the samples. This could demonstrate the capability of this biosensor to detect the SARS-CoV-2 RNA virus without the need for an extraction step.

3.4. Reproducibility and stability of the biosensor

The reproducibility of the created biosensor was explored by utilizing five identical MXene/Pt/C/GCE for 1 pM synthetic target. The relative standard deviation (RSD) value was 2.39%, thus demonstrating the adequate repeatability of the sensing technique. In addition, stability of the created sensor was assessed. The sensing system was stored in a refrigerator (4 °C) and measured for a period of 45 days as part of further research. The signal maintained 103.7% of the initial signal after 45 days with an RSD of 2%, thus demonstrating the acceptable stability of the biosensor (Fig. S5).

The constructed DNA sensor offers numerous advantages over other biosensors presented in Table S3. Firstly, the implementation of a signal amplifier composed of MXene/Pt/C nanocomposite has significantly increased sensitivity levels to attomolar concentrations without resorting to costly methods such as reverse transcription or nucleic acid amplification that require laboratory transport and cell extractors. Secondly, this biosensor was able to accurately quantify targets at low concentration levels (60–70 copies/mL) across various matrices including clinical RNA samples from nasopharyngeal swabs, serum and saliva with large sample sizes up to 192 individuals. Statistical analysis using T-tests and ROC demonstrated its ability for distinguishing between positive/negative groups with high accuracy rates comparable with electrochemical sensors listed on Table S3. Furthermore, three patients were tested utilizing nasopharyngeal samples without complete extraction procedures which highlights potential applications towards pathogenic virus detection through an easy-to-use point-of-care test format. Future development of this technology is looking towards real point-of-care tests for high-throughput capabilities diagnostics.

4. Conclusion

This study described the development of a DNA sensor based on GCE decorated by MXene/Pt/C/GCE nanocomposite and DNA/RNA hybridization method for detection of COVID-19. The suggested sensing platform demonstrated excellent specificity, sensitivity, low LOD of 0.4 aM, and LOQ of 60 copies/mL. 100% accuracy and sensitivity and 98% specificity for SARS-CoV-2 RNAs, which were isolated from 192 clinical samples, within only 30 min were achieved. The biosensor could differentiate SARS-CoV-2 from the different subtypes of clinical samples of various subtypes of influenza with high selectivity. Additionally, it could serve as a useful diagnostic method for detection of SARS-CoV-2 infection in various sample matrices, including nasopharyngeal swabs, serum, and saliva samples, which indicate this developed-nanobiosensor can be utilized in creating new and effective detection reproducible and stable methods due to its easy, quick, accurate, low cost and straightforward setup.

Declaration of competing interest

The authors declare that they have no known competing financial interests or personal relationships that could have appeared to influence the work reported in this paper.

Data availability

The authors are unable or have chosen not to specify which data has been used.

Acknowledgment

Mashhad University of Medical Sciences(MUMS) provided financial support for this study (Grant number: 991960). This report has been extracted from the MSc thesis of Monireh Bolourinezhad.

Appendix A. Supplementary data

Supplementary data to this article can be found online at https://doi.org/10.1016/j.talanta.2023.124804.

References

[1] J. Cui, F. Li, Z.-L. Shi, Origin and evolution of pathogenic coronaviruses, Nat. Rev. Microbiol. 17 (3) (2019) 181–192.
[2] W. Wu, A. Wang, M. Liu, Clinical features of patients infected with 2019 novel coronavirus in Wuhan, China, Lancet 395 (10223) (2020) 497–506.
[3] M.J. Loeffelholz, Y.-W. Tang, Laboratory diagnosis of emerging human coronavirus infections–the state of the art, Emerg. Microb. Infect. 9 (1) (2020) 747–756.
[4] V.M. Corman, O. Landt, M. Kaiser, R. Molenkamp, A. Meijer, D.K. Chu, T. Bleicker, S. Brünink, J. Schneider, M.L. Schmidt, Detection of 2019 novel coronavirus (2019-nCoV) by real-time RT-PCR, Euro Surveill. 25 (3) (2020), 2000045.
[5] T. Kilic, R. Weissleder, H. Lee, Molecular and immunological diagnostic tests of COVID-19: current status and challenges, iScience 23 (8) (2020), 101406.
[6] Y.-W. Tang, J.E. Schmitz, D.H. Persing, C.W. Stratton, Laboratory diagnosis of COVID-19: current issues and challenges, J. Clin. Microbiol. 58 (6) (2020), e00512-e00520.
[7] A. Scohy, A. Anantharajah, M. Bodéus, B. Kabamba-Mukadi, A. Verroken, H. Rodriguez-Villalobos, Low performance of rapid antigen detection test as frontline testing for COVID-19 diagnosis, J. Clin. Virol. 129 (2020), 104455.

[8] O. Filchakova, D. Dossym, A. Ilyas, T. Kuanysheva, A. Abdizhamil, R. Bukasov, Review of COVID-19 Testing and Diagnostic Methods, Talanta, 2022, 123409.

[9] M. Srivastava, N. Srivastava, P. Mishra, B.D. Malhotra, Prospects of nanomaterials-enabled biosensors for COVID-19 detection, Sci. Total Environ. 754 (2021), 142363.

[10] M. Khan, M. Hasan, S. Hossain, M. Ahommed, M. Daizy, Ultrasensitive detection of pathogenic viruses with electrochemical biosensor: state of the art, Biosens. Bioelectron. 166 (2020), 112431.

[11] A. Merkoçi, C.-z. Li, L.M. Lechuga, A. Ozcan, Editorial on COVID-19 biosensing technologies-2d Edition, Biosens. Bioelectron. 212 (2022), 114340.

[12] A. Yakoh, U. Pimpitak, S. Rengpipat, N. Hirankarn, O. Chailapakul, S. Chaiyo, Based electrochemical biosensor for diagnosing COVID-19: detection of SARS-CoV-2 antibodies and antigen, Biosens. Bioelectron. 176 (2021), 112912.

[13] Y. Tepeli, A. Ülkü, Electrochemical biosensors for influenza virus a detection: the potential of adaptation of these devices to POC systems, Sensor. Actuator. B Chem. 254 (2018) 377–384.

[14] G. Kim, J. Kim, S.M. Kim, T. Kato, J. Yoon, S. Noh, E.Y. Park, C. Park, T. Lee, J.-W. Choi, Fabrication of MERS-nanovesicle biosensor composed of multi-functional DNA aptamer/graphene-MoS2 nanocomposite based on electrochemical and surface-enhanced Raman spectroscopy, Sensor. Actuator. B Chem. 352 (2022), 131060.

[15] F. Ansah, F. Krampa, J.K. Donkor, C. Owusu-Appiah, S. Ashitei, V.E. Kornu, R. K. Danku, J.D. Chirawurah, G.A. Awandare, Y. Aniweh, Ultrasensitive electrochemical genosensors for species-specific diagnosis of malaria, Electrochim. Acta 429 (2022), 140988.

[16] X. Zha, W. Qin, J. Chen, M. Chen, Q. Zhang, K. He, Y. Liu, W. Liu, Anchoring red blood cell with tetrahedral DNA nanostructure: electrochemical biosensor for the sensitive signage of circulating tumor DNA, Talanta 251 (2023), 123793.

[17] M. Ali, M. Bacchu, S. Das, S. Akter, M. Rahman, M.A.S. Aly, M. Khan, Label free flexible electrochemical DNA biosensor for selective detection of Shigella flexneri in real food samples, Talanta 253 (2023), 123909.

[18] Y.-Y. Li, L.-J. Yue, L.-H. Yue, L. Jia, J.-Q. Liu, K.-F. Xie, X.-Y. Yang, Y.-H. Zhang, Metal-organic frameworks-derived hollow nanotube La2O3-In2O3 heterojunctions for enhanced TEA sensing at low temperature, Sensor. Actuator. B Chem. 378 (2023), 133125.

[19] M. Li, J. Zheng, X. Wang, R. Yu, Y. Wang, Y. Qiu, X. Cheng, G. Wang, G. Chen, K. Xie, Light-responsive self-strained organic semiconductor for large flexible OFET sensing array, Nat. Commun. 13 (1) (2022) 4912.

[20] X. Yang, Y. Shi, K. Xie, S. Fang, Y. Zhang, Y. Deng, Cocrystallization enabled spatial self-confinement approach to synthesize crystalline porous metal oxide nanosheets for gas sensing, Angew. Chem. 134 (37) (2022), e202207816.

[21] F. Wei, P.B. Lillehoj, C.-M. Ho, DNA diagnostics: nanotechnology-enhanced electrochemical detection of nucleic acids, Pediatr. Res. 67 (5) (2010) 458–468.

[22] M. Bacchu, M. Ali, S. Das, S. Akter, H. Sakamoto, S.-I. Suye, M. Rahman, K. Campbell, M. Khan, A DNA functionalized advanced electrochemical biosensor for identification of the foodborne pathogen Salmonella enterica serovar Typhi in real samples, Anal. Chim. Acta 1192 (2022), 339332.

[23] F. Otero, K. Shortall, U. Salaj-Kosla, S.A. Tofail, E. Magner, Electrochemical biosensor for the detection of a sequence of the TP53 gene using a methylene blue labelled DNA probe, Electrochim. Acta 388 (2021), 138642.

[24] D. Tyagi, H. Wang, W. Huang, L. Hu, Y. Tang, Z. Guo, Z. Ouyang, H. Zhang, Recent advances in two-dimensional-material-based sensing technology toward health and environmental monitoring applications, Nanoscale 12 (6) (2020) 3535–3559.

[25] L. Fan, J.J. Huang, J. Liao, Competitive smartphone-based portable electrochemical aptasensor system based on an MXene/cDNA-MB probe for the determination of Microcystin-LR, Sensor. Actuator. B Chem. (2022), 132164.

[26] X. Song, H. Gao, R. Yuan, Y. Xiang, Trimetallic nanoparticle-decorated MXene nanosheets for catalytic electrochemical detection of carcinoembryonic antigen via Exo III-aided dual recycling amplifications, Sensor. Actuator. B Chem. 359 (2022), 131617.

[27] M. Chen, N. Gan, T. Li, Y. Wang, Q. Xu, Y. Chen, An electrochemical aptasensor for multiplex antibiotics detection using Y-shaped DNA-based metal ions encoded probes with NMOF substrate and CSRP target-triggered amplification strategy, Anal. Chim. Acta 968 (2017) 30–39.

[28] N. Gao, F. Gao, S. He, Q. Zhu, J. Huang, H. Tanaka, Q. Wang, Graphene oxide directed in-situ deposition of electroactive silver nanoparticles and its electrochemical sensing application for DNA analysis, Anal. Chim. Acta 951 (2017) 58–67.

[29] R. Zhou, B. Tu, D. Xia, H. He, Z. Cai, N. Gao, G. Chang, Y. He, High-performance Pt/Ti3C2Tx MXene based graphene electrochemical transistor for selective detection of dopamine, Anal. Chim. Acta 1201 (2022), 339653.

[30] X. Zhu, B. Liu, H. Hou, Z. Huang, K.M. Zeinu, L. Huang, X. Yuan, D. Guo, J. Hu, J. Yang, Alkaline intercalation of Ti3C2 MXene for simultaneous electrochemical detection of Cd (II), Pb (II), Cu (II) and Hg (II), Electrochim. Acta 248 (2017) 46–57.

[31] X. Wang, M. Li, S. Yang, J. Shan, A novel electrochemical sensor based on TiO2–Ti3C2TX/CTAB/chitosan composite for the detection of nitrite, Electrochim. Acta 359 (2020), 136938.

[32] P.K. Kalambate, N.S. Gadhari, X. Li, Z. Rao, S.T. Navale, Y. Shen, V.R. Patil, Y. Huang, Recent advances in MXene–based electrochemical sensors and biosensors, TrAC, Trends Anal. Chem. 120 (2019), 115643.

[33] H. Wang, H. Li, Y. Huang, M. Xiong, F. Wang, C. Li, A label-free electrochemical biosensor for highly sensitive detection of gliotoxin based on DNA nanostructure/MXene nanocomplexes, Biosens. Bioelectron. 142 (2019), 111531.

[34] J. Yoon, M. Shin, J. Lim, J.-Y. Lee, J.-W. Choi, Recent advances in MXene nanocomposite-based biosensors, Biosensors 10 (11) (2020) 185.

[35] K.S. Bhat, S. Byun, A. Alam, M. Ko, J. An, S. Lim, A fast and label-free detection of hydroxymethylated DNA using a nozzle-jet printed AuNPs@ Ti3C2 MXene-based electrochemical sensor, Talanta 244 (2022), 123421.

[36] J. Zhao, C. He, W. Wu, H. Yang, J. Dong, L. Wen, Z. Hu, M. Yang, C. Hou, D. Huo, MXene-MoS2 heterostructure collaborated with catalyzed hairpin assembly for label-free electrochemical detection of microRNA-21, Talanta 237 (2022), 122927.

[37] T.R. Abbott, G. Dhamdhere, Y. Liu, X. Lin, L. Goudy, L. Zeng, A. Chemparathy, S. Chmura, N.S. Heaton, R. Debs, Development of CRISPR as an antiviral strategy to combat SARS-CoV-2 and influenza, Cell 181 (4) (2020) 865–876, e12.

[38] T.A. Hall, BioEdit: a User-Friendly Biological Sequence Alignment Editor and Analysis Program for Windows 95/98/NT, Nucleic Acids Symposium Series, Information Retrieval Ltd., [London, 1999, pp. 95–98, c1979-c2000.

[39] C.W. Wong, T.J. Albert, V.B. Vega, J.E. Norton, D.J. Cutler, T.A. Richmond, L. W. Stanton, E.T. Liu, L.D. Miller, Tracking the evolution of the SARS coronavirus using high-throughput, high-density resequencing arrays, Genome Res. 14 (3) (2004) 398–405.

[40] P. Bogner, I. Capua, D.J. Lipman, N.J. Cox, A global initiative on sharing avian flu data, Nature 442 (7106) (2006), 981-981.

[41] S. Han, W. Liu, S. Yang, R. Wang, Facile and label-free electrochemical biosensors for microRNA detection based on DNA origami nanostructures, ACS Omega 4 (6) (2019) 11025–11031.

[42] Y. Wu, S. Ali, R.J. White, Electrocatalytic mechanism for improving sensitivity and specificity of electrochemical nucleic acid-based sensors with covalent redox tags—Part I, ACS Sens. 5 (12) (2020) 3833–3841.

[43] C. Pina-Coronado, Á. Martínez-Sobrino, L. Gutiérrez-Gálvez, R. Del Caño, E. Martínez-Periñán, D. García-Nieto, M. Rodríguez-Peña, M. Luna, P. Milán-Rois, M. Castellanos, Methylene Blue functionalized carbon nanodots combined with different shape gold nanostructures for sensitive and selective SARS-CoV-2 sensing, Sensor. Actuator. B Chem. 369 (2022), 132217.

[44] M. Naguib, M. Kurtoglu, V. Presser, J. Lu, J. Niu, M. Heon, L. Hultman, Y. Gogotsi, M.W. Barsoum, Two-dimensional nanocrystals produced by exfoliation of Ti3AlC2, Adv. Mater. 23 (37) (2011) 4248–4253.

[45] F. Wang, C. Yang, M. Duan, Y. Tang, J. Zhu, TiO2 nanoparticle modified organ-like Ti3C2 MXene nanocomposite encapsulating hemoglobin for a mediator-free biosensor with excellent performances, Biosens. Bioelectron. 74 (2015) 1022–1028.

[46] Y. Chen, P.-X. Yuan, A.-J. Wang, X. Luo, Y. Xue, L. Zhang, J.-J. Feng, A novel electrochemical immunosensor for highly sensitive detection of prostate-specific antigen using 3D open-structured PtCu nanoframes for signal amplification, Biosens. Bioelectron. 126 (2019) 187–192.

[47] M. Mahmood, A. Rasheed, I. Ayman, T. Rasheed, S. Munir, S. Ajmal, P.O. Agboola, M.F. Warsi, M. Shahid, Synthesis of ultrathin MnO2 nanowire-intercalated 2D-MXenes for high-performance hybrid supercapacitors, Energy Fuel. 35 (4) (2021) 3469–3478.

[48] K.S. Rizi, B. Hatamluyi, M. Rezayi, Z. Meshkat, M. Sankian, K. Ghazvini, H. Farsiani, E. Aryan, Response surface methodology optimized electrochemical DNA biosensor based on HAPNPTs/PPY/MWCNTs nanocomposite for detecting Mycobacterium tuberculosis, Talanta 226 (2021), 122099.

[49] B. Hatamluyi, M. Rezayi, S.A. Jamehdar, K.S. Rizi, M. Mojarrad, Z. Meshkat, H. Choobin, S. Soleimanpour, M.T. Boroushaki, Sensitive and specific clinically diagnosis of SARS-CoV-2 employing a novel biosensor based on boron nitride quantum dots/flower-like gold nanostructures signal amplification, Biosens. Bioelectron. 207 (2022), 114209.

[50] D. Chen, D. Wang, X. Hu, G. Long, Y. Zhang, L. Zhou, A DNA nanostructured biosensor for electrochemical analysis of HER2 using bioconjugate of GNR@ Pd SSs—apt—HRP, Sensor. Actuator. B Chem. 296 (2019), 126650.

[51] B. Hatamluyi, F. Lorestani, Z. Es'haghi, Au/Pd@ rGO nanocomposite decorated with poly (L-Cysteine) as a probe for simultaneous sensitive electrochemical determination of anticancer drugs, Ifosfamide and Etoposide, Biosens. Bioelectron. 120 (2018) 22–29.

[52] M. Manzano, S. Viezzi, S. Mazerat, R.S. Marks, J. Vidic, Rapid and label-free electrochemical DNA biosensor for detecting hepatitis A virus, Biosens. Bioelectron. 100 (2018) 89–95.

[53] L. Fabiani, M. Saroglia, G. Galatà, R. De Santis, S. Fillo, V. Luca, G. Faggioni, N. D'Amore, E. Regalbuto, P. Salvatori, Magnetic beads combined with carbon black-based screen-printed electrodes for COVID-19: a reliable and miniaturized electrochemical immunosensor for SARS-CoV-2 detection in saliva, Biosens. Bioelectron. 171 (2021), 112686.

[54] Z. Song, Y. Ma, M. Chen, A. Ambrosi, C. Ding, X. Luo, Electrochemical biosensor with enhanced antifouling capability for COVID-19 nucleic acid detection in complex biological media, Anal. Chem. 93 (14) (2021) 5963–5971.

[55] W.L. Ang, R.R.X. Lim, A. Ambrosi, A. Bonanni, Rapid electrochemical detection of COVID-19 genomic sequence with dual-function graphene nanocolloids based biosensor, FlatChem 32 (2022), 100336.

[56] M. Alafeef, K. Dighe, P. Moitra, D. Pan, Rapid, ultrasensitive, and quantitative detection of SARS-CoV-2 using antisense oligonucleotides directed electrochemical biosensor chip, ACS Nano 14 (12) (2020) 17028–17045.

[57] H. Liu, E. Dai, R. Xiao, Z. Zhou, M. Zhang, Z. Bai, Y. Shao, K. Qi, J. Tu, C. Wang, Development of a SERS-based lateral flow immunoassay for rapid and ultra-sensitive detection of anti-SARS-CoV-2 IgM/IgG in clinical samples, Sensor. Actuator. B Chem. 329 (2021), 129196.